SIAM J. SCI. COMPUT.
Vol. 38, No. 6, pp. B917–B940

LARGE-SCALE THREE-DIMENSIONAL ACOUSTIC HORN OPTIMIZATION*

STEPHAN SCHMIDT†, EDDIE WADBRO‡, AND MARTIN BERGGREN‡

Abstract. We consider techniques that enable large-scale gradient-based shape optimization of wave-guiding devices in the context of three-dimensional time-domain simulations. The approach relies on a memory efficient boundary representation of the shape gradient together with primal and adjoint solvers semiautomatically generated by the FEniCS framework. The hyperbolic character of the governing linear wave equation, written as a first-order system, is exploited through systematic use of the characteristic decomposition both to define the objective function and to obtain stable numerical fluxes in the discontinuous Galerkin spatial discretization. The methodology is successfully used to optimize the shape of a midrange acoustic horn, described by 1,762 design variables, for maximum transmission efficiency, where the parallel computations involve a total of 3.5×10^9 unknowns.

Key words. shape optimization, shape derivatives, acoustic wave equation, computational acoustics, discontinuous Galerkin method, code generation

AMS subject classifications. 35L05, 65K10, 65M25, 65M32, 68N19

DOI. 10.1137/15M1021131

1. Introduction.

Horn-like structures appear in devices for both acoustic and electromagnetic waves. A horn serves as an interface between a waveguide or a radiation source and the surrounding space and provides both impedance matching to the source and directivity control of the transmission. These properties are utilized in a variety of applications. The *bell* in brass instruments constitutes a part of a resonator—the air space within the instrument—and the bell shape is judiciously designed to constrain the most important resonances to integer frequency ratios. Recently, there have been some efforts to use numerical shape optimization in order to design brass bells so that the instrument acquires prescribed resonance characteristics [8, 20]. A type of acoustic *inverse horn*, that is, a device that possesses a large diameter at the source and a small one at the outlet, is used in ultrasonic machining, a subtractive manufacturing process particularly suitable for hard and brittle materials [1]. Horn *loudspeakers*, which are at focus here, are routinely used to supply the mid- and high-frequency range in public address systems for large halls, cinemas, and outdoors, often assembled in the form of so-called line arrays [34]. A horn dramatically raises the efficiency of the radiating source and may be used for precise directional control of the coverage area. In spite of its advantages, horn-equipped loudspeakers are often viewed as subpar with respect to sound quality [10, sect. 4.9]. However, some of the sound-quality deficiencies of horns may be due to suboptimal design and not to inherent limitations of the concept of acoustical horns.

The use of simple, classical shapes, such as exponentials, and the classical analysis of wave motion in horns, based on the one-dimensional (1D) Webster horn equation [19], is rapidly being complemented with more accurate numerical methods, which allow

*Submitted to the journal's Computational Methods in Science and Engineering section May 12, 2015; accepted for publication (in revised form) August 1, 2016; published electronically November 1, 2016.

http://www.siam.org/journals/sisc/38-6/M102113.html

†Department of Mathematics, University of Würzburg, 970 74 Würzburg, Germany (stephan.schmidt@uni-wuerzburg.de, https://www.mathematik.uni-wuerzburg.de/∼schmidt/).

‡Department of Computing Science, Umeå University, SE–901 87 Umeå, Sweden (eddiew@cs.umu.se, martin.berggren@cs.umu.se).

analysis of much more complex shapes. During the last decade or so, a number of studies have appeared that use optimization algorithms together with numerical solutions of the governing equation to design acoustic horns [3, 4, 6, 13, 16, 31, 32]. It turns out that detailed shaping of the horn flare by the use of numerical shape optimization methods can produce horns with much more favorable input impedance properties compared to those associated with classical shapes such as exponentials, as also has been confirmed by measurements on manufactured prototypes [21]. The difference in input impedance properties between simple and optimized shapes is quite large, particularly at the low end of the operational frequency range. Unfavorable input impedance properties will give rise to acoustic resonances in the horn, and the typical "honky" megaphone-like sound associated with horns could be due to such resonances. We believe that there is therefore a great potential in the use of optimization to design horns with much less of such coloring. Some studies consider the directivity properties of the horn in the optimization process [18, 30, 33] instead of, or in addition to, the input impedance. All the above-mentioned studies employ frequency-domain modeling and are confined to 2D geometries, which means that only cylindrical (or laterally infinite) horns can be considered. However, in practice, it is important to be able to separately control the vertical and horizontal directivity properties, which will necessitate full 3D acoustic models. Moreover, since the radiation properties of horns ideally should be uniform throughout their operational range, frequency-domain methods need to be run at a large number of frequencies. It may therefore be beneficial to consider time-domain methods, where only one equation needs to be solved at each design cycle. The frequency content for which the horn should be optimized is then controlled by selecting a suitable input pulse.

In contrast to previous work, our aim here is to apply numerical shape optimization for *detailed design* of an acoustic horn in *three dimensions* using a *time-domain model* of the acoustic wave propagation. We consider here only the impedance-matching aspect, setting the stage for future treatment of more complex problems, such as optimizing with respect to directivity properties. The linear wave equation written in first-order form models the wave propagation. The hyperbolic nature of the equations is respected through the use of a discontinuous Galerkin spatial discretization with upwinding fluxes based on a characteristic decomposition [14]. The characteristic decomposition is also used to define the objective function.

Since we rely on gradient-based optimization and the adjoint-variable method for the sensitivity analysis, the computational complexity for each gradient evaluation is independent of the number of design variables. We use this property to be able to control the shape in detail; each mesh point on the horn's surface is subject to design, and a smoothing strategy is utilized to promote smooth design updates. For efficiency, both computationally and with respect to implementation effort and maintainability of the software, we make use of the FEniCS [17] suite to generate the primal and dual solver for acoustic analysis. The gradient expression used by the optimization routine is assembled from the primal and adjoint solutions using an expression derived from the equations in integral form. This approach yields a boundary-integral representation for the objective function gradient, which means that the gradient expression requires only the time history of the primal and adjoint solutions restricted to the design surface, and not everywhere in the computational domain, which would be extremely memory demanding for a time-domain calculation. The necessity to differentiate the mesh deformation procedure is likewise eliminated by this approach.

The paper is structured as follows. In section 2, we review the governing equations and the concept of characteristic decomposition, which is central to this application.

Sections 3 and 4 introduce the objective function and the resulting first-order optimality system. The discretization scheme is presented in section 5, and results from cross-code verification studies are given in section 6. Finally, section 7 presents results of a large-scale intrinsically 3D horn optimization.

2. Acoustic power balance and the characteristic decomposition. We use the concept of a *characteristic decomposition* of the acoustic power flux over surfaces extensively throughout the following. The concept, which is briefly reviewed in this section, is used to define physical boundary conditions, lay out the objective function of optimization, and specify interelement fluxes in the numerical scheme.

Acoustic wave propagation in still air under the conditions of uniform static density and temperature is governed by the linear wave equation

$$\frac{\partial u}{\partial t} + \nabla p = 0, \tag{1a}$$

$$\frac{\partial p}{\partial t} + c^2 \mathrm{div}\, u = 0, \tag{1b}$$

where p denotes the acoustic pressure; u the acoustic momentum density vector, that is, the product of the static air density and the acoustic velocity vector; and c the speed of sound.

For each open, bounded domain D in space, solutions to system (1) satisfy the conservation law

$$\frac{d}{dt}\frac{1}{2}\int_D \|u\|^2 + \frac{1}{c^2}p^2\, dx = -\int_{\partial D} p\langle u, n\rangle\, d\Gamma, \tag{2}$$

where n is the outward-directed unit normal on ∂D, $\langle\,\cdot\,,\,\cdot\,\rangle$ denotes the Euclidean inner product, and $\|u\|^2 = \langle u, u\rangle$. Conservation law (2) says that the time derivative of the acoustic energy in D equals the net flux of acoustic power[1] into D through boundary ∂D. Conservation law (2) is obtained by taking the dot product of equation (1a) with u, multiplying equation (1b) by p/c^2, summing the equations, integrating, and using the divergence theorem.

The integrand on the right-hand side of conservation law (2) can be split up into a difference of two positive terms as follows:

$$\begin{aligned} -p\langle u, n\rangle &= \frac{1}{c}\left(\frac{1}{2}\left(p - c\langle u, n\rangle\right)\right)^2 - \frac{1}{c}\left(\frac{1}{2}\left(p + c\langle u, n\rangle\right)\right)^2 \\ &= \frac{1}{c}\left(w_-^2 - w_+^2\right), \end{aligned} \tag{3}$$

where

$$w_\pm = \frac{1}{2}\left(p \pm c\langle u, n\rangle\right) \tag{4}$$

are called the *characteristic variables*. By substituting the splitting (3) into conservation law (2), we find that

$$\frac{d}{dt}\frac{1}{2}\int_D \|u\|^2 + \frac{1}{c^2}p^2\, dx = \frac{1}{c}\int_{\partial D} w_-^2 - w_+^2\, d\Gamma, \tag{5}$$

[1] To obtain the correct dimensions of power, the terms in equation (2) should be divided by the static air density.

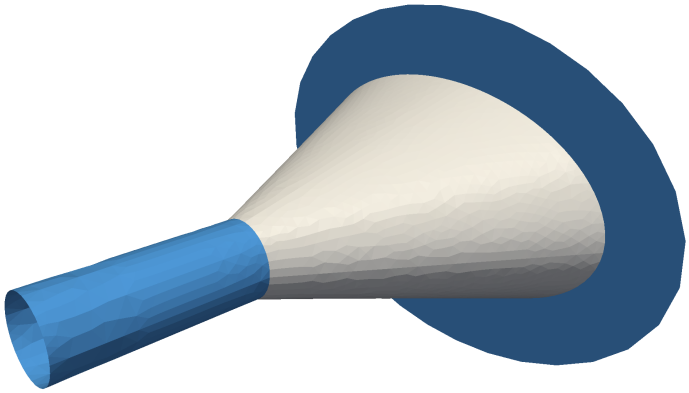

FIG. 1. *The geometry for the model problem comprises a horn that on one side is mounted in an infinite baffle and on the other side attached to a waveguide. Variable horn flare in light gray, fixed wave-guide and baffle in blue (color online). Surrounding domain Ω not shown.*

which reveals that the use of characteristic variables yields a splitting of the power flux over ∂D into the acoustic power that flows *into* the domain D (integral of w_-^2) and the the power that flows *out* of the domain (integral of w_+^2). The plus and the minus subscripts in the characteristic variables indicate the direction in relation to the (outward-directed) normal n on ∂D.

3. The model problem. We consider the 3D setup illustrated in Figure 1. To reduce the computational cost, we will compute on only a quarter of the domain. This setup consists of a waveguide attached to the throat of an acoustic horn that is mounted in an infinite baffle. We denote by Γ_{wall} the sound-hard walls of the waveguide, the acoustic horn, and the baffle, and by Γ_{symm} the symmetry boundaries. For numerical reasons, we truncate the domain and denote the truncated computational domain by Ω. The boundary $\partial\Omega$ can be decomposed as the closure of $\Gamma_{\text{wall}} \cup \Gamma_{\text{symm}} \cup \Gamma_{\text{in}} \cup \Gamma_{\text{out}}$, where the two latter parts stem from the truncation of the computational domain. More precisely, Γ_{in} truncates the waveguide, and Γ_{out} is the boundary that truncates the free-space in front of the horn. The acoustic initial–boundary-value problem we consider is

$$
\begin{aligned}
\frac{\partial u}{\partial t} + \nabla p &= 0 && \text{in } \Omega \text{ for } t > 0,\\
\frac{\partial p}{\partial t} + c^2 \operatorname{div} u &= 0 && \text{in } \Omega \text{ for } t > 0,\\
\frac{1}{2}\left(p - c\langle u, n\rangle\right) &= g && \text{on } \Gamma_{\text{in}} \text{ for } t > 0,\\
\frac{1}{2}\left(p - c\langle u, n\rangle\right) &= 0 && \text{on } \Gamma_{\text{out}} \text{ for } t > 0,\\
\langle u, n\rangle &= 0 && \text{on } \Gamma_{\text{wall}} \cup \Gamma_{\text{symm}} \text{ for } t > 0,\\
u &\equiv 0 && \text{in } \Omega \text{ at } t = 0,\\
p &\equiv 0 && \text{in } \Omega \text{ at } t = 0,
\end{aligned}
\tag{6}
$$

where g is a given function with compact support in time. From the discussion in section 2, we see that the boundary condition on Γ_{in} sets the incoming characteristic (w_-) to be equal to the given function g, and the boundary condition on Γ_{out} ensures

that no incoming acoustic power is transmitted into Ω from the exterior. The condition of a sound-hard material is imposed through the boundary condition on Γ_{wall}. The zero normal velocity condition also imposes the symmetry condition at Γ_{symm}.

Applying the power balance law (5) on solutions to system (6) under the specified boundary conditions, we find that

$$\frac{d}{dt}\frac{1}{2}\int_\Omega \|u\|^2 + \frac{1}{c^2}p^2\,dx = \frac{1}{c}\int_{\Gamma_{\text{in}}} g^2 - w_+^2\,d\Gamma - \frac{1}{c}\int_{\Gamma_{\text{out}}} w_+^2\,d\Gamma, \tag{7}$$

where we have made use of the characteristic variables as defined in expression (4).

Since we assume that the input g has compact support in time, it holds for an "open" system like this one that the solution will vanish identically after a sufficiently long time T, which is consistent with the fact that the right-hand side of conservation law (7) becomes negative when $g \equiv 0$. Thus, integrating expression (7) over a sufficiently long time interval $(0, T)$, utilizing the initial condition $u(0) = 0$ and $p(0) = 0$ and the vanishing assumption $u(T) = 0$ and $p(T) = 0$, we find that

$$\int_0^T \int_{\Gamma_{\text{in}}} g^2\,d\Gamma = \int_0^T \int_{\Gamma_{\text{in}}} w_+^2\,d\Gamma + \int_0^T \int_{\Gamma_{\text{out}}} w_+^2\,d\Gamma. \tag{8}$$

Expression (8) states the basic energy balance of system (6): the total acoustic energy of the input signal (left-hand side) equals the energy of the reflected signal (first term on the right-hand side) plus the energy transmitted to the surroundings (second term on the right-hand side). Thus, to maximize the total transmitted energy, we may equivalently minimize the reflected signal, which will be simpler to do in a numerical implementation.

Here, we let the shape of boundary Γ_{horn}, colored light gray in Figure 1, be subject to design. The beginning and the end of the horn flare will be fixed, so that the optimization can change neither the mouth and throat shapes nor the length of the horn. Each such admissible horn shape will generate a candidate computational domain Ω, for which we solve state equation (6) and evaluate the objective function

$$J(\Omega) = \frac{1}{2}\int_0^T \int_{\Gamma_{\text{in}}} (p + \langle u, n\rangle)^2\,d\Gamma\,dt, \tag{9}$$

integrated for a sufficiently long time T with respect to the time support of the input signal g. The optimization problem can then be formulated as

$$\begin{gathered}\min J(\Omega) \text{ subject to} \\ \text{state equation (6).}\end{gathered} \tag{10}$$

If the final design is such that the objective function, that is, the reflected signal, vanishes for the given input signal, then the *input impedance* at the throat of the horn is real and constant for each of the frequencies contained in the signal. (For a discussion of the relation between reflections, which is the measure we use here, and the concept of acoustic impedance, we refer the reader to the acoustics literature, for instance Rienstra and Hirschberg's lecture notes [22, sect. 3.2].) This approach is appropriate for transmission optimization of a horn in isolation, as here. However, if a model of the wave source, typically a *compression driver* in the case of a mid- or high-frequency horn, is available, it would also be possible to maximize the total transmitted acoustic power for the coupled system driver–horn.

4. Domain variations and optimality system. Conceptually, design problem (10) is a PDE-constrained optimization problem with the added difficulty that there is a need to associate with the shape of Γ_{horn} a suitable set of decision variables in the optimization algorithm. There are several possible choices. One possibility is to introduce an artificial inhomogeneous static density function into the governing equations, so that regions of sound-hard materials are approximated using a dense fluid. This approach transforms the problem from one using a varying domain to one that involves a variable coefficient in the governing equations [5, 27, 32]. Another possibility is to use an explicit parameterization of feasible domain shapes through, for instance, a finite set of smooth ansatz functions [15]. Here, we consider domain deformations that are assumed to be generated by a sufficiently smooth vector field $V : \mathbb{R}^3 \to \mathbb{R}^3$. This approach can be exploited to derive a computationally efficient boundary representation of the shape derivative, a property related to the so-called Hadamard–Zolésio structure theorem [11, 28].

A boundary representation of the shape gradient allows for very efficient numerical schemes utilizing the maximum degrees of freedom by exercising the position of every surface vertex as a design parameter. Furthermore, all terms stemming from a deformation of the mesh and those related to the differentiation of the PDE solution procedure with respect to the input mesh are treated on an analytic level, thereby circumventing the need to actually compute them on a discrete level. The resulting methodology is independent of the actual PDE solver, and the sensitivities can be computed using any methodology to solve the state equation, provided an adjoint is also available. The applicability of this approach to large-scale 3D problems in aerodynamics was, for example, considered previously in [25].

The appendix carries out the shape sensitivity analysis for optimization problem (10) with state equation (6) written in a suitable integral form. To obtain the final boundary representation for the shape derivative, quite delicate conditions on the regularity of the solution have to be assumed, as indicated in the appendix. Such high regularity does not hold for typical finite-element functions, which means that the boundary representation of the shape derivative, as derived in the appendix, will not be fully consistent with a differentiation of the objective function actually used after discretization [7], [11, Remark 2.3]. However, this gap in consistency is usually reduced as the mesh is refined, an effect also visible in our finite difference verification in section 6.2.

For the studied problem, the admissible shape changes of Γ_{horn} are generated through a smooth vector field $V : \mathbb{R}^3 \to \mathbb{R}^3$ that vanishes everywhere on $\partial\Omega$ except on Γ_{horn}. After a sensitivity analysis, as outlined in the appendix, we find that the shape derivative of objective function (9) with respect to V has the boundary representation

$$dJ(\Omega)[V] = 2c \int_0^T \int_{\Gamma_{\text{horn}}} \langle V, n\rangle \operatorname{div}(up^*)\, d\Gamma\, dt, \tag{11}$$

where u solves system (6) and p^* the adjoint system

$$\begin{aligned}
-\frac{\partial u^*}{\partial t} + \nabla p^* &= 0 && \text{in } \Omega \text{ for } t < T,\\
-\frac{\partial p^*}{\partial t} + c^2 \operatorname{div} u^* &= 0 && \text{in } \Omega \text{ for } t < T,\\
\frac{1}{2}\left(p^* - c\langle u^*, n\rangle\right) &= \frac{1}{2}\left(p + c\langle u, n\rangle\right) && \text{on } \Gamma_{\text{in}} \text{ for } t < T,
\end{aligned} \tag{12}$$

$$\begin{aligned} \frac{1}{2}\,(p^* - c\langle u^*, n\rangle) &= 0 && \text{on } \Gamma_{\text{out}} \text{ for } t < T, \\ \langle u^*, n\rangle &= 0 && \text{on } \Gamma_{\text{wall}} \cup \Gamma_{\text{symm}} \text{ for } t < T, \\ u^* \equiv 0, \qquad p^* &\equiv 0 && \text{in } \Omega \text{ at } t = T. \end{aligned}$$

We note that the adjoint system (12) after the variable change $t \mapsto T - t$ equals the state equation (6) with $w_+(T-t)|_{\Gamma_{\text{in}}}$ instead of $g(t)$ as source. That is, the state and adjoint systems are the same, but the state equation is driven by the given source function g, and the adjoint equation by the time convolution of the reflected signal at the inlet.

5. Spatial discretization. To introduce the variational form that is the basis for our discontinuous Galerkin discretization, we consider an open, bounded, and connected set $K \subset \Omega$, representing what later will be an element in our triangulation. Assume that u and p satisfy system (6). Multiplying the first and second equations in system (6) with arbitrary smooth test functions v and q, respectively, integrating over K, and integrating by parts in space, we find that $u(t)|_K$ and $p(t)|_K$ satisfy

$$\int_K \langle v, \partial_t u\rangle - p\ \text{div}\ v + q\ \partial_t p - c^2\langle u, \nabla q\rangle\, dx + \int_{\partial K} \langle v, n\rangle p + c^2\langle u, n\rangle q\, d\Gamma = 0 \tag{13}$$

for each pair of smooth test functions v and q with support in K. Next, we introduce the *flux functions*

$$\begin{aligned} f_1(u, p, n) &:= np = n(w_+ + w_-), \\ f_2(u, p, n) &:= c\langle u, n\rangle = (w_+ - w_-), \end{aligned} \tag{14}$$

which, as we see above, can be written in terms of sums and differences of the characteristic variables (4), a property that will be exploited below to define the numerical flux functions. Using definitions (14), equation (13) can be written as

$$\int_K \langle v, \partial_t u\rangle - p\ \text{div}\ v + q\ \partial_t p - c^2\langle u, \nabla q\rangle\, dx + \int_{\partial K} \langle v, f_1\rangle\ + c\, q f_2\, d\Gamma = 0. \tag{15}$$

Now introduce a triangulation $\mathscr{T}_h$ of the domain Ω consisting of nonoverlapping open tetrahedrons K such that $\overline{\Omega} = \cup_{K\in\mathscr{T}_h} \overline{K}$. The numerical scheme is defined by requiring $p(t)$ and the components of vector $u(t)$ to be functions whose restrictions on each K are polynomials that satisfy a modified version of variational expression (15) for all polynomial test functions v and q. Since p and u will then in general possess jump discontinuities over each interface between two neighboring elements, the question is what values to use in the flux functions f_1, f_2, since they are evaluated exactly where the functions are discontinuous. A standard choice that leads to a consistent and stable scheme is *upwinding*. This method exploits the directivity information in the characteristic variables and uses the *local* values in K in the *outgoing* characteristic variable w_+ and the *remote* values—from neighboring cells or from the boundary conditions—in the *incoming* characteristic variable w_-. More precisely, let $\mathcal{P}_r$ define the space of polynomials of maximum degree r. For each $K \in \mathscr{T}_h$ we require $u(t)|_K \in P_r^3$, $p(t)|_K \in P_r$ such that for each $v \in P_r^3$, $q \in P_r$,

$$\int_K \langle v, \partial_t u\rangle - p\ \text{div}\ v + q\ \partial_t p - c^2\langle u, \nabla q\rangle\, dx + \int_{\partial K} \langle v, f_1^*\rangle\ + c\, q f_2^* d\Gamma = 0, \tag{16}$$

where the *upwind numerical flux functions* are defined by

$$
\begin{aligned}
f_1^* &:= n(w_+^L + w_-^R) = n\left[\frac{1}{2}\left(p^L + p^R\right) + \frac{c}{2}\left(\langle u^L, n\rangle - \langle u^R, n\rangle\right)\right], \\
f_2^* &:= w_+^L - w_-^R = \frac{1}{2}\left(p^L - p^R\right) + \frac{c}{2}\left(\langle u^L, n\rangle + \langle u^R, n\rangle\right),
\end{aligned} \tag{17}
$$

where the superscripts L and R denote local and remote values. The local values are given by the values of $u|_K$ and $p|_K$ on ∂K. The remote values are given either in order to assign boundary conditions, if ∂K coincides with the boundary, or by the values of $u|_{K'}$ and $p|_{K'}$, if there is a neighboring $K' \in \mathcal{T}_h$ such that $\overline{K'} \cap \overline{K} \subset \partial K$, that is, we are at a face that is shared between K and K'. The term "upwind" for the flux function (17) is borrowed from fluid mechanics and is motivated by the fact that the characteristic variables are evaluated according the direction of power transport across ∂K.

By imposing the remote states

$$
\begin{aligned}
u^R &:= -\frac{1}{c} g n, \quad p^R := g \quad \text{on } \Gamma_{\text{in}}, \\
u^R &:= 0, \qquad\quad p^R := 0 \quad \text{on } \Gamma_{\text{out}},
\end{aligned} \tag{18}
$$

we see that the incoming characteristic w_-^R on Γ_{in} and Γ_{out} will be set to the correct values as specified by system (6).

Since we compute on only a quarter of the horn, we impose that the solution should be symmetric across planes Γ_{symm}. The symmetry and sound-hard boundary condition $\langle u, n\rangle = 0$ is here imposed by the custom numerical flux function

$$
f_{1,\text{ws}}^* = n p^L, \qquad f_{2,\text{ws}}^* = 0, \tag{19}
$$

which can be motivated by substituting condition $\langle u, n\rangle = 0$ into the exact flux functions (14). An alternative strategy to impose condition $\langle u, n\rangle = 0$ is to use the upwind flux (17) and specify a remote state that mirrors the local state according to the formula $u^R := u^L - 2\langle u^L, n\rangle n$ and $p^L := p^R$ on Γ_{symm}. However, in the numerical experiments below, we have chosen the explicit wall flux function (19), since this choice will lead to a boundary integral over Γ_{horn} in the variational form whose integrand is *linear* in the wall normal. This property is consistent with the choice made to enforce the wall boundary condition in the integral form used for sensitivity analysis, equation (40), and leads to a much simpler expression for the shape gradient compared to the case when mirroring the local state; see the discussion in Appendix A.1.

To specify the complete scheme, based on the discussion above, we need a number of definitions. Let $S = \bigcup_{k=1}^{M} S_m$ be the union of all open triangular element faces S_m that are shared between two elements, that is, the set of element faces that are not part of the boundary. For each such internal element face S_m, it holds that $\overline{S}_m = \partial K_{m_1} \cap \partial K_{m_2}$ for some distinct neighboring elements K_{m_1}, $K_{m_2} \in \mathcal{T}_h$. We denote by n_{m_1}, $n_{m_2} = -n_{m_1}$ the outward-directed unit normals to K_{m_1} and K_{m_2} on S_m. For each piecewise-polynomial f, we define $f_1 = f|_{K_{m_1}}$, $f_2 = f|_{K_{m_2}}$, and the face-sum and face-jump operators

$$
\begin{aligned}
\{\{ f \}\} &:= f_1|_{S_m} + f_2|_{S_m}, \\
[\![f]\!] &:= \begin{cases} n_{m_1} f_1|_{S_m} + n_{m_2} f_2|_{S_m} & \text{if } f \in \mathbb{R}, \\ \langle n_{m_1}, f_1|_{S_m}\rangle + \langle n_{m_2}, f_2|_{S_m}\rangle & \text{if } f \in \mathbb{R}^3. \end{cases}
\end{aligned} \tag{20}
$$

Moreover, we define $\Omega_0 := \Omega \setminus \overline{S}$ and the function

$$\hat{g} := \begin{cases} g & \text{on } \Gamma_{\text{in}}, \\ 0 & \text{on } \Gamma_{\text{out}}. \end{cases} \tag{21}$$

Now we sum equation (16) over all $K \in \mathscr{T}_h$, utilizing the upwind flux (17) over the element interfaces, imposing the remote states (18) and the wall/symmetry fluxes (19). We then obtain that $u(t) \in P_r^3(\mathscr{T}_h)$, $p(t) \in P_r(\mathscr{T}_h)$ satisfy

$$\begin{aligned} &\int_{\Omega_0} \langle v, \partial_t u \rangle - p \operatorname{div} v + q\, \partial_t p - c^2 \langle u, \nabla q \rangle \, dx + \int_{\Gamma_{\text{wall}} \cup \Gamma_{\text{symm}}} \langle v, np \rangle \, d\Gamma \\ &+ \int_{\Gamma_{\text{in}} \cup \Gamma_{\text{out}}} \left\langle v, n \left[\hat{g} + \frac{1}{2}(p + c\langle u, n \rangle) \right] \right\rangle + cq \left[\frac{1}{2}(p + c\langle u, n \rangle) - \hat{g} \right] d\Gamma \\ &\quad + \frac{1}{2} \int_S [\![v]\!] \big(\{\!\{ p \}\!\} + c [\![u]\!] \big) \, d\Gamma + \frac{1}{2} \int_S c \big\langle [\![q]\!], \big([\![p]\!] + c \{\!\{ u \}\!\} \big) \big\rangle \, d\Gamma = 0 \end{aligned} \tag{22}$$

for each $v \in P_r^3(\mathscr{T}_h)$, $q \in P_r(\mathscr{T}_h)$.

6. Implementation and verification.

6.1. Verification of the forward solver. Variational problem (22) is implemented numerically using the FEniCS environment [17], which contains a domain-specific language for variational problems. After postulating the variational expression in Python, a C/C++ discontinuous Galerkin solver of the desired spatial order is automatically generated and compiled by the FEniCS environment. Time derivatives are discretized by the trapezoidal method. (A completely explicit low storage fourth-order Runge–Kutta scheme is also implemented, but this scheme behaves problematically if the mesh quality degrades too much during shape optimization when the mesh is deformed.) The implicit equation to solve for each time-step is linear. Depending on available compute power, spatial order, and mesh refinement, we first attempt to factorize the system once and store this factorization for all time-steps. If this is not tractable, for example due to excessive storage requirements, we solve the implicit equation for each time-step using restarted GMRES with ILU preconditioning, a functionality provided by PETSc and Hypre.

In the frequency domain, a horn's radiation efficiency can be characterized by its *reflection coefficient* at the throat, which for each frequency measures the (complex-valued) quotient between the pressure amplitude of an incoming single frequency wave and the reflected wave's pressure amplitude. To verify our implementation, we compute the reflection coefficient spectrum with our code as well as with Comsol Multiphysics on the cylindrically symmetric domain illustrated in Figure 2. Here, the width and length of the waveguide are set to $a = 19.3$ mm and $d = 100$ mm, respectively. The length of the conical horn flare is $l = 150$ mm, and the half width of the horn mouth is $b = 100$ mm. For all simulations, the speed of sound is $c = 345$ m/s.

The baseline for the verification computations is carried out with Comsol in the frequency domain. That is, we consider single-frequency wave propagation with angular frequency $\omega = 2\pi f$, where f is the ordinal frequency. We use the ansatz $p(x,t) = \operatorname{Re}\{\tilde{p}_\omega(x) \mathrm{e}^{\mathrm{i}\omega t}\}$ and solve the following boundary-value problem [30] for the

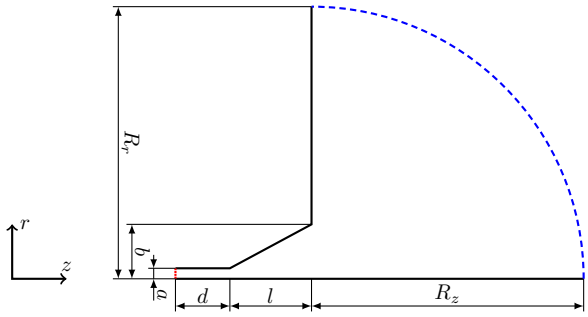

FIG. 2. *Cross section of the cylindrically symmetric geometry used for the initial computations.*

complex amplitude function $\tilde{p}_\omega$:

$$
\begin{aligned}
\frac{\partial}{\partial r}\left(\frac{1}{r}\frac{\partial \tilde{p}_\omega}{\partial r}\right) + \frac{\partial}{\partial z}\left(\frac{1}{r}\frac{\partial \tilde{p}_\omega}{\partial z}\right) + k^2 r \tilde{p}_\omega &= 0 && \text{in } \Omega^{(2\mathrm{D})},\\
\left(\mathrm{i}k\tilde{p}_\omega + \frac{1}{R}\right)\tilde{p}_\omega + \frac{\partial \tilde{p}_\omega}{\partial n} &= 0 && \text{on } \Gamma_{\text{out}}^{(2\mathrm{D})},\\
\mathrm{i}k\tilde{p} + \frac{\partial \tilde{p}_\omega}{\partial n} &= 2\mathrm{i}kA && \text{on } \Gamma_{\text{in}}^{(2\mathrm{D})},\\
\frac{\partial \tilde{p}_\omega}{\partial n} &= 0 && \text{on } \Gamma_{\text{horn}}^{(2\mathrm{D})} \cup \Gamma_{\text{symm}}^{(2\mathrm{D})},
\end{aligned}
\tag{23}
$$

where $k = \omega/c$. The boundary conditions on $\Gamma_{\text{in}}^{(2\mathrm{D})}$ and $\Gamma_{\text{out}}^{(2\mathrm{D})}$ are frequency-domain analogues of characteristic boundary conditions used in the discontinuous Galerkin code at corresponding boundaries. The condition on $\Gamma_{\text{in}}^{(2\mathrm{D})}$ imposes a planar right-going wave with amplitude A while absorbing planar left-going waves. At $\Gamma_{\text{out}}^{(2\mathrm{D})}$, the boundary condition absorbs any outgoing waves propagating in the normal direction with respect to the boundary. The reflection coefficient is given by

$$
R_\omega^{(2D)} = \frac{2}{a^2 A}\int_{\Gamma_{\text{in}}^{(2\mathrm{D})}} r(\tilde{p}_\omega - A)\, d\Gamma. \tag{24}
$$

For the 3D time domain discontinuous Galerkin computation, we use a truncated sinc pulse as input signal,

$$
g(t) = \frac{\sin\big(2\pi f_s(t-t_c)\big)}{2\pi f_s(t-t_c)} \sin\big(2\pi f_c(t-t_c)\big) w(t,t_c), \tag{25}
$$

where t_c is the time around which the pulse is centered, f_c is the desired center frequency, f_s is the half bandwidth of the signal, and $w(t,t_c)$ is a window function. Here, we set $t_c = 3/(2f_s)$ and use the Hamming window function

$$
w(t,t_c) = \begin{cases} 0.54 + 0.46\cos\left(\frac{\pi(t-t_c)}{t_c}\right) & \text{for } t \in [0, 2t_c],\\ 0 & \text{otherwise.}\end{cases} \tag{26}
$$

Without a window function, the spectrum of the time-infinite sinc pulse is flat within $[f_c - f_s, f_c + f_s]$ and zero outside. The use of a window function converts the infinite

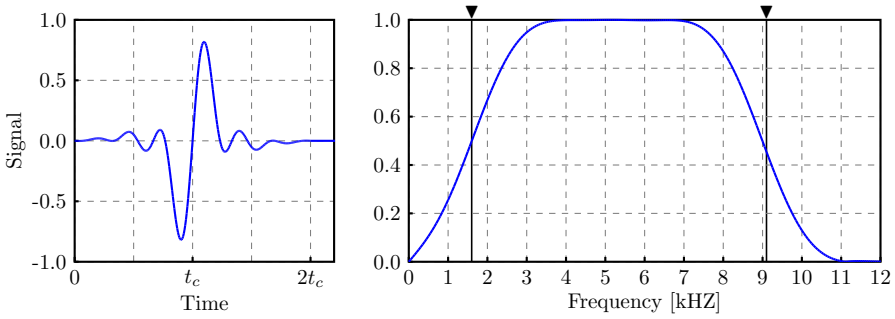

FIG. 3. *Left: The input signal as a function of time. Right: The magnitude spectrum of the input signal for $f_c = 5.3$ kHz, $f_s = 3.7$ kHz, and $t_c = 3/7400$ s. The solid vertical lines mark the frequencies $f_c \pm f_s$ that limit the frequency range in the following figures showing the reflection spectra.*

signal to a signal of finite duration but also impacts the spectrum. In all numerical experiments using the time domain solver, we use an input signal with parameters $f_c = 5.3$ kHz and $f_s = 3.7$ kHz. Figure 3 illustrates the input signal as a function of time (left diagram) and its normalized magnitude spectrum computed by the discrete Fourier transform (DFT) (right diagram).

For the baseline 2D Comsol simulations, the radius of the computational domain is $R = R_z = R_r = 1500$ mm, and we use continuous piecewise-quadratic elements on a triangular mesh with maximum side length 10 mm, which yields 97,769 unknowns for the linear system. We carry out the 3D time domain verification simulations on a cylindrical symmetric horn model in quarter symmetry, using discontinuous piecewise-linear elements on two different unstructured tetrahedral meshes, a fine and a crude resolution mesh.

The fine resolution mesh uses $R_z = 240$ mm, $R_r = 220$ mm and consists of $114,417$ elements, which yields a total of $(3+1) \cdot 4 \cdot 114,417 = 1,830,672$ unknowns per time-step. The shortest edge in the mesh is 0.78 mm, the longest is 29.65 mm, and the average is 5.46 mm. As a comparison, note that the wavelength at 9 kHz is about 38 mm. For the fine resolution mesh, we use the end time $T = 18$ ms and the time-step $dt = 5.0 \cdot 10^{-7}$. The crude resolution mesh uses $R_z = 80$ mm and $R_r = 140$ mm and consists of 8,356 elements, which yields 133,696 unknowns per time-step. The shortest edge in this mesh is 2.51 mm, the longest edge is 36.16 mm, and the average is 9.22 mm. Here, the end time $T = 4.5$ ms, and the time-step $dt = 2.5 \cdot 10^{-6}$.

The initial 3D experiments focus on studying the transient behavior of the wave propagation and the decay of energy inside the domain. For our input signal, these experiments confirm that the acoustic energy inside the domain is exponentially decreasing, and we conclude that after about 4 ms—corresponding approximately to 10 t_c—the energy inside the computational domain is less then 10^{-6} of the energy of the input pulse. (Here, the energy inside the computational domain is evaluated as the difference between the numerically evaluated left- and right-hand sides of energy balance (8).) We also experimented with different time-steps for the implicit time stepper and found that the above mentioned $dt = 2.5 \cdot 10^{-6}$ provides a good trade-off between computational effort and accuracy for the standard resolution mesh.

During the time domain simulations, we record the outgoing signal at Γ_{in}. After the simulation is completed, we compute the spectrum of the outgoing signal using the

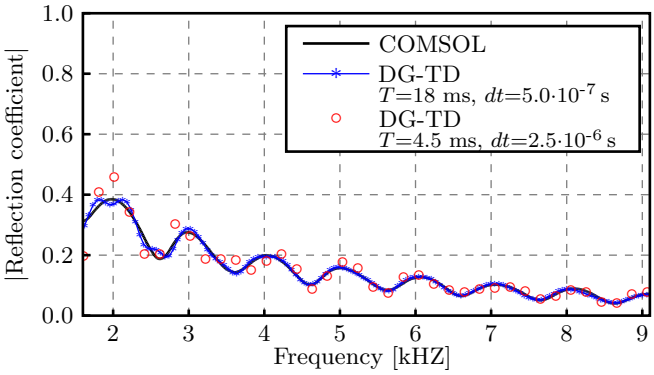

FIG. 4. *Magnitude reflection spectra in the range* 1.6–9.1 *kHz for the cylindrical symmetric horn depicted in Figure* 2 *with parameters* $a = 19.3$ *mm,* $b = d = 100$ *mm, and* $l = 150$ *mm. Solid black line: Comsol Multiphysics using FD-FEM in* 2*D cylindrical symmetry,* 10 *Hz frequency spacing. Line with asterisks: our* 3*D TD-DG code, fine resolution. Circular markers: our* 3*D TD-DG code, standard resolution.*

DFT. The reflection coefficient spectrum at the horn's throat can then be computed by pointwise division of the Fourier coefficients of the input signal and the reflected signal. Figure 4 shows the magnitude of the reflection coefficient versus frequency computed by Comsol Multiphysics for the cylindrically symmetric frequency domain setup (solid line) and by our discontinuous Galerkin 3D time domain method on the two different meshes. The spectrum computed using the fine-mesh fully 3D time domain method agrees well with the reference computation, and we note that the use of a too-crude mesh tends to overestimate variations in the reflection coefficient, which is likely due to a too-crude and nonsmooth approximation of the horn geometry.

6.2. Finite difference verification of the shape derivative. Following the previous verification of the solver, we next verify the shape derivatives computed by (51) and (52) against finite difference approximations. The geometry is as in the previous section, and we again perform the test using two different meshes and far-field locations. For each vertex x_i on the design boundary, we define a vector-valued perturbation function $V_i : \Gamma_{\text{horn}} \to \mathbb{R}^3$ by

$$V_i(x) = \phi_i(x) n_{\text{vertex}}(x_i),$$

where ϕ_i is the linear Lagrangian basis function (the standard "hat" function centered at x_i). Thus, V_i equals the vertex normal at vertex x_i; it has support only within $\text{Patch}(x_i)$, the surface patch formed around x_i, and it vanishes outside this patch. We compute each component of the adjoint-based directional derivative via (51) and (52) by integrating

$$dJ_1 := dJ(\Gamma_{\text{horn}})[V_i] = 2c \int_0^T \int_{\text{Patch}(x_i)} \langle V_i, n_{\text{facet}} \rangle \operatorname{div}(up^*)\, d\Gamma\, dt,$$

$$dJ_2 := dJ(\Gamma_{\text{horn}})[V_i] = 2c \int_0^T \int_{\text{Patch}(x_i)} \langle V_i, n_{\text{facet}} \rangle \operatorname{div}(u^*p)\, d\Gamma\, dt.$$

Note that for the adjoint-based directional derivative, the primal and dual states need to be computed only once on the unperturbed geometry. To compute the adjoint,

we restrict the storage of the primal state to a tubular neighborhood of two cells around Γ_{wall}, which reduces the memory demand for the primal trajectory considerably yet still allows for a correct computation of the source term in the adjoint and the divergence operator constituting the gradient. Due to the similarity of the primal and dual equations, we can easily re-use most components of the primal solver. The same strategy is used during optimization.

For the finite difference computation used for verification purposes, we extend a damped perturbation $\tau \cdot V_i$ into the domain by solving a noncoupled componentwise Laplace equation for the displacement of the mesh vertices, as we also do during the optimization to deform the volume mesh. We use $\tau = 10^{-4}$ as the constant finite difference step length. The objective function (9) is evaluated on both the perturbed and original grids in order to calculate a one-sided finite difference.

As in the preceding section, we verify both formulas on two different meshes, the crude resolution mesh with a close far-field boundary ($R_z = 80$ mm and $R_r = 140$ mm) and a fine resolution mesh with the far-field boundary further away ($R_z = 240$ mm and $R_r = 220$ mm). However, the fine resolution mesh is here derefined once, compared to the mesh used in previous section, to keep the compute time for the finite difference verification manageable. Thus, we consider either 698 design variables on the crude mesh ("mesh 1") or $1,236$ design variables on a finer mesh ("mesh 2"). The results are shown in Table 1. As expected, the difference between dJ_1 and dJ_2 is marginal; we thus focus on dJ_1 here. As discussed in section 4, there are quite restrictive regularity assumptions necessary for a consistent shape derivative. Nevertheless, the higher resolution of the finer mesh shows a direct increase in consistency under mesh refinement, and the results indicate that the quality of the gradient more than suffices to compute reasonable descent directions if the mesh is fine enough.

TABLE 1
Finite difference (FD) verification of the shape derivative (SD).

	Mesh 1	Mesh 2
Cells	$8,356$	$49,648$
Vertices	$2,337$	$11,232$
Variable vertices	698	$1,236$
ℓ_2-norm SD	0.01404	0.01315
ℓ_2-norm FD	0.01353	0.01276
ℓ_2-norm error	0.00125	0.00062
ℓ_∞-norm SD	0.00378	0.00408
ℓ_∞-norm FD	0.00365	0.00376
ℓ_∞-norm error	0.00050	0.00032
ℓ_1-norm SD	0.11000	0.11293
ℓ_1-norm FD	0.10821	0.11109
ℓ_1-norm error	0.00821	0.00499

7. Optimization.

7.1. Preliminaries. When using a boundary representation for the shape derivative, a steepest descent algorithm for the shape optimization problem at hand can simply be implemented by

$$\Gamma_{\text{horn}}^{k+1} = \{x - \epsilon \cdot G(x) \cdot n(x) : x \in \Gamma_{\text{horn}}^{k}\}, \tag{27}$$

where ϵ is the step length of the gradient descent scheme, k denotes the iteration counter, and the normal derivative of the objective with respect to shape perturbations

can be identified from expression (52), that is,

$$G(x) = \int_0^T 2c \ \mathrm{div}\left(p(t,x)\, u^*(t,x)\right)\, dt. \tag{28}$$

Due to the boundary formulation, no additional calculations, such as the potentially computationally costly derivative of the mesh deformation process, are necessary. Any mesh deformation or remeshing approach can be used, and they are interchangeable without the need to consider additional derivatives.

However, there are some geometric considerations that have not been addressed so far. First, we would like to steer the optimization towards smooth updates in order not to be trapped in local optima with bad performance [3] and in order to obtain manufacturable shapes. Second, we would like the horn to attach properly to the waveguide and end at a prescribed mouth shape. The latter condition prevents the optimization from gradually elongating the horn; generally, the longer the horn is, the easier it is to reduce the reflections, particularly in the low end of the target spectrum. Both these conditions can be addressed simultaneously by calculating a smoothed descent direction G_s through the solution of

$$\begin{aligned} (-\delta\Delta_\Gamma + I)\cdot G_s &= G \qquad \text{on } \Gamma_{\text{horn}}, \\ G_s &= 0 \qquad \text{on } \partial\Gamma_{\text{horn}}, \end{aligned} \tag{29}$$

where Δ_Γ denotes the surface or tangential Laplacian, I is the identity, and $\delta = 0.1$ is a parameter controlling the amount of gradient smoothing. Since the left-side operator in equation (29) is positive definite, G_s is a descent direction if G is. More details on the effect of this gradient smoothing procedure can be found, for example, in [2, 26, 29]. The zero Dirichlet boundary condition in problem (29) is applied for nodes on the throat interface between horn and waveguide as well as for nodes on edges constituting the mouth, fixing those edges as discussed above.

Although the use of G_s in the optimization algorithm yields smooth updates and forces the horn to attach to the throat and the mouth, it does not necessarily lead to a good discretization of the unknown surface, meaning that very often surface nodes start to cluster, thereby creating a poor discretization and low quality discontinuous Galerkin mesh, possibly with inverted surface elements. The descent direction (52) is invariant under tangential modifications of V. Therefore, we can use the excess degree of freedom in the tangent plane to reparametrize the discretization of the surface by moving nodes in tangential direction $r_1(x)\cdot\tau_1(x) + r_2(x)\cdot\tau_2(x)$, where $\tau_i(x)$ describes a consistent choice of basis vectors of the tangent plane at x and $r_i(x) \in \mathbb{R}$, such that a locally even spacing of vertices is achieved in each optimization iteration. Such a tangential reparameterization is achieved by successively moving the surface vertices to the centroid of the corresponding Voronoi cell of the dual mesh, projected into the tangent plane. Because the centroidal Voronoi tessellation (CVT) can be interpreted as the dual of the Delaunay triangulation [9, 12], this approach can be thought of as turning the Delaunay remeshing procedure into a mesh deformation scheme by only relocating nodes but not changing connectivity. More information on the reparameterization and mesh deformation approach can be found in [24]. After ensuring the quality of the surface tessellation, the volume mesh is made to match the new horn boundary by solving a noncoupled componentwise Laplace equation for the mesh node displacements with a dampening coefficient of 0.1. Deforming the volume mesh offers several advantages over remeshing, because element connectivities and consequently the memory structure and adjoint data flow remain unchanged.

Summarizing the above, we conduct a gradient descent by first computing the new discretized boundary via the new node positions

$$\Gamma_{\text{horn}}^{k+1} := \{x - \epsilon \cdot G_s(x) \cdot n(x) + r_1(x) \cdot \tau_1(x) + r_2(x) \cdot \tau_2(x) : x \in \Gamma_{\text{horn}}^{k}\}, \tag{30}$$

and we afterwards make the volume mesh match this boundary by solving uncoupled Laplace equations for the mesh node displacements in the volume. Thus, based on the current surface mesh Γ_{horn}^{k}, we apply a descent step in the normal direction together with a tangential reparameterization, such that the nodes of $\Gamma_{\text{horn}}^{k+1}$ adhere to the CVT criterion, making equation (30) partly implicit with respect to determining $r_i(x)$. This procedure works without an analytic description of the surface, such as B-splines or NURBS, which would be necessary for a redistribution via remeshing, and our scheme works completely on the discretized level.

As a stopping criterion, we use the size of the $L^2(\Gamma_{\text{horn}})$-norm of the smoothed gradient, a condition that yields a first-order necessary condition, including the geometric constraints at throat and mouth, and that also measures the actual deformation not including the tangential repair.

7.2. Numerical results. We demonstrate the feasibility of our methodology by an application to a large-scale horn optimization problem of practical relevance and of a kind that cannot be substituted by a 2D problem. To this end, we consider a horn that blends a circular throat of 19.3 mm radius (same as in the verification) into an elliptic mouth with half-axes 100 mm and 60 mm, respectively. The throat dimension is suitable for mounting a standard 1.5 inch compression driver, a type of sound source that is standard for midrange acoustic horns, and the elliptic mouth is chosen to obtain a priori directivity differences in the horizontal and vertical directions. The blending between throat and mouth is linear for the starting geometry. The sinc pulse—and therefore the spectrum to optimize for—is the same as for the validation calculations above.

We use a high density mesh surpassing the quality of the finest mesh, "Mesh 2," from the finite difference and the forward solver verification tests by using $121,631$ cells and a total of $25,118$ vertices for a physically smaller geometry. Thus, the shortest edge is 1.1984 mm, the longest edge is 19.9922 mm, and the average edge length is 5.8856 mm. Physical dimensions are again the same as in "Mesh 2" from the finite difference validation, except that the mouth of the horn is not circular but ellipsoidal, with the vertical radius of the opening scaled to 60%. This leads to the optimization of $1,762$ node positions constituting the mantle surface. Using a time-step of $2.5 \cdot 10^{-6}$ seconds, we operate at roughly 40% of the maximum step length allowed by the CFL criterion. Each simulation then conducts $1,798$ time-steps until an end time of $4.4975 \cdot 10^{-3}$ seconds. This amounts to $1,946,096$ quarter domain state unknowns per time-step, or $3,499,080,608$ unknowns to be determined in total. To compute the adjoint forcing and the shape derivative, we reduce this data to $437,992,800$ unknowns by utilizing the boundary representation of the shape derivative, not storing unnecessary volume data. Thus, for each optimization step, we have to be able to handle at least 3.26 GB of double precision data instead of 26 TB for the full trajectory, excluding additional RAM necessary for the preconditioned Krylov solvers needed to solve the implicit system at each time-step. The optimization is conducted fully parallel on 48 cores of a four-node Intel Xeon E5-2630 workstation running at a clock speed of 2.30 GHz, which results in roughly 40 minutes total wall clock time per optimization iteration. Beginning from an objective function value of $J = 5.875 \cdot 10^{-7}$ and an initial L^2-norm of the smoothed gradient of $2.889 \cdot 10^{-5}$, we need $1,789$ optimization steps until the

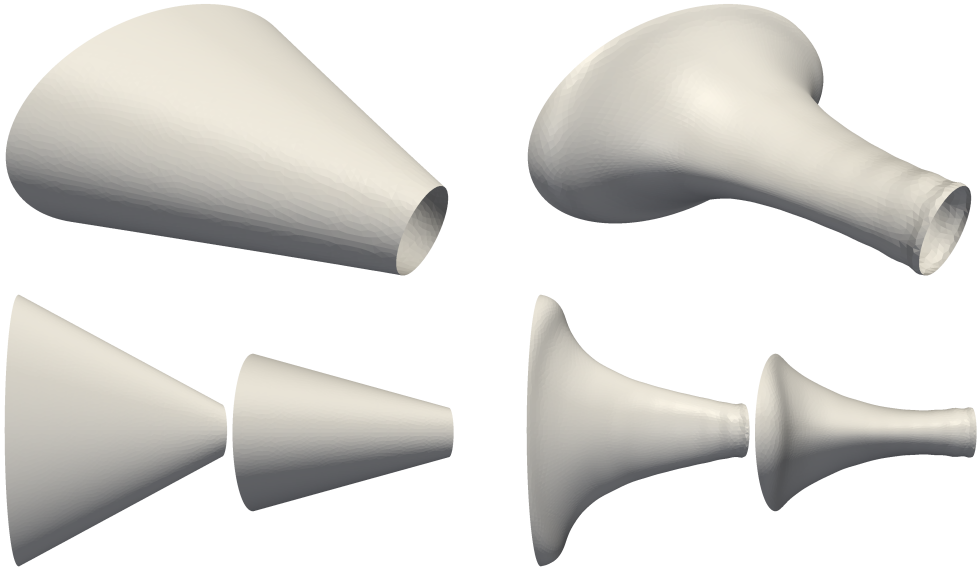

FIG. 5. *Isoperimetric, top, and side views of the elliptic test-case. Starting guess to the left, and final shape to the right.*

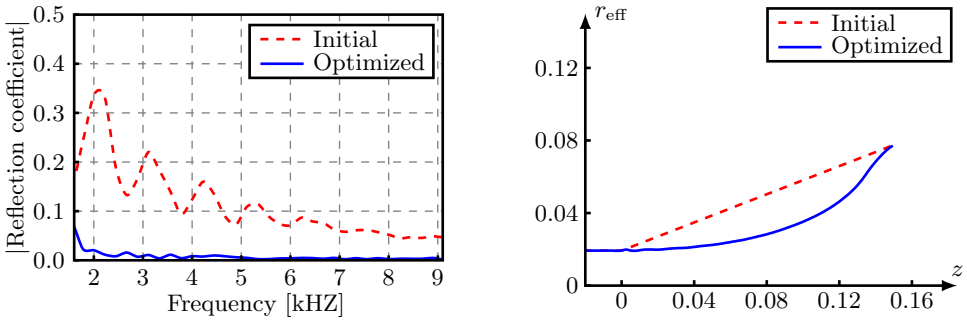

FIG. 6. *Left: Magnitude reflection spectra of the initial (dashed lines) as well as the optimized (solid lines) horn. Right: Effective radii of the initial (dashed lines) as well as the optimized (solid lines) horn.*

L^2-norm of the smoothed gradient falls below $1.5 \cdot 10^{-8}$, terminating at an objective function value of $J = 6.048 \cdot 10^{-9}$. In total, the optimization required a total of roughly $57,248$ CPU hours, including parallel overhead. Figure 5 shows the initial (left) as well as the optimized (right) horn shapes.

Magnitude reflection spectra are shown in Figure 6. The spectrum of the optimized horn with its nonintuitive shape is a substantial improvement over the initial geometry over the whole frequency band prescribed by the incoming sinc pulse, with some frequencies actually having a reflection coefficient of almost zero. Figure 6 also shows the effective radii, that is, the radii that would give cylindrically symmetric horns of the same cross-sectional area as the one considered here. The optimized horn's cross-sectional area grows in the axial direction and avoids the sharp edge at the throat, which the initial horn exhibits. The behavior of the effective radii changes character a few centimeters from the horn mouth (approximately at $z = 0.13$ m) where the

effective radius quickly increases and then levels out. This is most likely an interesting end effect that stems from the imposed fixed rim of the horn mouth.

8. Discussion and outlook. To the best of our knowledge, this is the first time that numerical shape optimization has been used for detailed design of an acoustic horn using full 3D time domain modeling. The characteristic decomposition of the acoustic power density is a key ingredient in our approach; it is used both to define the objective function for the optimization and to obtain stable numerical fluxes in the numerical method. Another key ingredient is the surface representation of the objective function gradient, which limits the need for storage of time histories of the primal and adjoint variables to layers of the design and inlet boundary. The alternative, to rely on exact gradients to the discrete objective function, would involve the time history of the fields throughout the domain, which would require excessive storage and would also necessitate access to derivatives of the mesh deformation scheme. In particular, for the mesh used here, our use of a surface representation of the gradient implies a data reduction from 26 TB to 3.26 GB. Smoothness requirements on the design updates as well as the fixed throat and mouth geometries are imposed through use of the Laplace–Beltrami operator.

Being able to optimize complex 3D geometries in a time-domain formulation will enable the consideration of more challenging objective functions in the future, such as impedance matching to a specific source and requirements on the far-field radiation pattern.

Appendix A. Sensitivity analysis.

A.1. Basic formulas. Let Ω denote an open and bounded domain in $\mathbb{R}^3$, and let $\Gamma \subset \partial\Omega$. We will differentiate integrals of the types

$$J_1(\Omega) = \int_\Omega f\,dx, \qquad J_2(\Omega) = \int_\Gamma h\,d\Gamma \tag{31}$$

with respect to domain variations generated by a smooth vector field $V : \mathbb{R}^3 \to \mathbb{R}^3$. A family of deformed domains Ω^ϵ and surfaces Γ^ϵ, parametrized by $\epsilon \geq 0$, are generated by the formula $x_\epsilon = x + \epsilon V(x)$ for $x \in \Omega$ or $x \in \Gamma$. We consider families of functions f_ϵ and h_ϵ defined on Ω^ϵ and Γ^ϵ, where $f = f_0$ and $h = h_0$, and define shape derivatives of integrals (31) as

$$dJ_1(\Omega)[V] = \lim_{\epsilon\to 0^+} \frac{1}{\epsilon}\left(\int_{\Omega^\epsilon} f_\epsilon\,dx - \int_\Omega f\,dx\right) =: \frac{d^+}{d\epsilon}\int_{\Omega^\epsilon} f_\epsilon\,dx\bigg|_{\epsilon=0}, \tag{32a}$$

$$dJ_2(\Omega)[V] = \lim_{\epsilon\to 0^+} \frac{1}{\epsilon}\left(\int_{\Gamma^\epsilon} h_\epsilon\,d\Gamma - \int_\Gamma h\,d\Gamma\right) =: \frac{d^+}{d\epsilon}\int_{\Gamma^\epsilon} h_\epsilon\,d\Gamma\bigg|_{\epsilon=0} \tag{32b}$$

if the limits exist. The *material derivative* of function families f_ϵ and h_ϵ at $\epsilon = 0$ is defined as

$$\dot f[V](x) = \lim_{\epsilon\to 0^+} \frac{f_\epsilon\big(x+\epsilon V(x)\big) - f(x)}{\epsilon}, \tag{33a}$$

$$\dot h[V](x) = \lim_{\epsilon\to 0^+} \frac{h_\epsilon\big(x+\epsilon V(x)\big) - h(x)}{\epsilon}, \tag{33b}$$

if the limits exist, and the *shape derivative* of the families is defined as

$$f'[V] = \dot f[V] - \big\langle V, \nabla f\big\rangle, \tag{34a}$$

$$h'[V] = \dot h[V] - \big\langle V, \nabla h\big\rangle. \tag{34b}$$

Remark 1. An often used alternative characterization of the shape derivative is the partial derivatives with respect to ϵ; that is, for fixed x, we have

$$f'[V](x) = \lim_{\epsilon \to 0} \frac{f_\epsilon(x) - f(x)}{\epsilon}, \tag{35a}$$

$$h'[V](x) = \lim_{\epsilon \to 0} \frac{h_\epsilon(x) - h(x)}{\epsilon}, \tag{35b}$$

which can be obtained by a Taylor expansion of f_ϵ and h_ϵ in definitions (33). However, a complicating factor with characterizations (35) is that the arguments of f_ϵ of h_ϵ in expressions (35) are not necessarily in the domains of definition Ω^ϵ, Γ^ϵ of the functions.

Sokolowski and Zolésio [28, sect. 2.31] prove the following formula for shape derivative (32a) under the assumptions that Ω is of class C^k, $k \geq 1$, and that f, $f'[V]$, and $\|\nabla f\|$ are all in $L^1(\Omega)$:

$$dJ_1(\Omega)[V] = \int_\Omega f'[V] + \operatorname{div}(Vf)\, dx = \int_\Omega f'[V]\, dx + \int_{\partial\Omega} \langle V, n\rangle f\, d\Gamma. \tag{36}$$

We will consider shape derivative (32b) in the following three cases:

(i) $\langle V, n\rangle \equiv 0$ on $\Gamma \subset \partial\Omega$.

(ii) $h(x) = \big\langle \tilde{h}(x), n(x)\big\rangle$, $\Gamma = \partial\Omega$, n is the outward-directed normal field on Γ, and $\tilde{h}$ is the trace of a vector-valued function in Ω whose divergence satisfies the conditions for f assumed for formula (36).

(iii) Conditions as for case (ii), but $\Gamma \subset \partial\Omega$ such that $\langle V, n\rangle \equiv 0$ on $\partial\Omega \setminus \Gamma$.

For these cases, the formula

$$dJ_2(\Omega)[V] = \begin{cases} \displaystyle\int_\Gamma h'[V]\, d\Gamma & \text{in case (i),} \\[2ex] \displaystyle\int_\Gamma \big\langle \tilde{h}'[V], n\big\rangle + \langle V, n\rangle \operatorname{div} \tilde{h}\, d\Gamma & \text{in cases (ii) and (iii)} \end{cases} \tag{37}$$

holds, where div $\tilde{h}$ inside the boundary integral denotes the trace on Γ of the divergence of $\tilde{h}$ in Ω. In case (i), $\Gamma^\epsilon = \Gamma$, so the formula follows immediately by definitions (33b) and (34b) as long as $h'[V]$ exists and is integrable. In case (ii), the divergence theorem and the substitution $f = \operatorname{div} \tilde{h}$ turn integral J_2 into a domain integral of J_1 type. Formula (37) then follows from expression (36) using the divergence theorem and the fact that the shape derivative and the spatial gradient commute. The formula for case (iii) follows from cases (i) and (ii).

Remark 2. Due to the particular integral form of the state equation used in Appendix A.2, the conditions of cases (i) and (ii) will be satisfied, and shape derivative formulas (36) and (37) are all that are needed. However, if the hard wall boundary condition on Γ_{horn} is imposed in a different way, for instance through an upwinding flux together with a remote mirrored state, as discussed in section 5, the linear structure assumed in cases (ii) and (iii) does not hold, and a formula admitting a more general form of the integrand h in integral J_2 is needed. A more general form is obtained by considering a family, parameterized by ϵ, of functions $\hat{h}_\epsilon$ defined on $\overline{\Omega}^\epsilon \times \overline{\Omega}^\epsilon$, and defining the integrand in J_2 to be $h_\epsilon(x_\epsilon) = \hat{h}_\epsilon(x_\epsilon, n_\epsilon(x_\epsilon))$ for $x_\epsilon \in \Gamma^\epsilon$. The shape derivative formula then becomes

$$dJ_2(\Omega)[V] = \int_\Gamma \hat{h}'[V] + \langle V, n\rangle \Big(\big\langle \nabla \hat{h}, n\big\rangle + \kappa\big(\hat{h} - \langle \nabla_y \hat{h}, n\rangle\big) + \operatorname{div}_\Gamma\big(\nabla_y \hat{h}\big)\Big)\, d\Gamma, \tag{38}$$

where κ is the local mean curvature, ∇ and div_Γ the gradient and the tangential divergence with respect to the first argument of $\hat{h}$, and ∇_y the gradient with respect to the second argument. Formula (38) is a special case of Lemma 3.3.14 in the first author's Ph. D. thesis [23]. To the best of our knowledge, this formula does not appear anywhere else in the open literature.

A.2. Shape derivatives and the adjoint system. We consider the objective function (9), where u, p satisfy initial–boundary-value problem (6). We require that the vector field V that generates the domain variations, as described above, vanishes on $\partial\Omega \setminus \Gamma_{\mathrm{horn}}$. This field V will generate a family of perturbed domains Ω^ϵ for which the horn boundary $\Gamma^\epsilon_{\mathrm{horn}}$ is perturbed. However, the rest of the boundary, $\partial\Omega \setminus \Gamma^\epsilon_{\mathrm{horn}}$, will be fixed independent of ϵ.

Differentiating objective function (9), using formula (37), and utilizing that V vanishes on Γ_{in}, we get

$$dJ(\Omega)[V] = \int_0^T \int_{\Gamma_{\mathrm{in}}} \big(p + c\langle u, n\rangle\big)\big(p'[V] + c\langle u'[V], n\rangle\big)\, d\Gamma\, dt. \tag{39}$$

In order to continue, we need to determine how the shape derivatives $p'[V]$, $u'[V]$ in expression (39) depend on V. We will therefore differentiate the state equation with respect to domain perturbations. To prepare for the use of formulas (36) and (37), we first rewrite state equation (6) in the integral form

$$\begin{aligned} c\int_\Omega \langle v, \partial_t u + \nabla p\rangle\, dx + \frac{1}{c}\int_\Omega q(\partial_t p + c^2 \mathrm{div}\, u)\, dx - c\int_{\Gamma_{\mathrm{s}}} q\langle u, n\rangle\, d\Gamma \\ + \frac{1}{2}\int_{\Gamma_{\mathrm{inout}}} (q - c\langle v, n\rangle)(p - c\langle u, n\rangle)\, d\Gamma = \int_{\Gamma_{\mathrm{in}}} (q - c\langle v, n\rangle) g\, d\Gamma, \end{aligned} \tag{40}$$

where $\Gamma_{\mathrm{s}} = \Gamma_{\mathrm{wall}} \cup \Gamma_{\mathrm{symm}}$ and $\Gamma_{\mathrm{inout}} = \Gamma_{\mathrm{in}} \cup \Gamma_{\mathrm{out}}$, and where v and q are arbitrary smooth test functions.

Remark 3. It is immediate, by inspection, that integral form (40) is *consistent* with system (6); that is, solutions to system (6) satisfy expression (40) for any smooth test functions. Moreover, integral form (40) is designed to satisfy a *stability* property, namely that the acoustic energy decreases with time when no input is provided to the systems. That is, for $g = 0$,

$$\frac{c}{2}\frac{d}{dt}\int_\Omega |u|^2\, dx + \frac{1}{2c}\frac{d}{dt}\int_\Omega p^2\, dx + \frac{1}{2}\int_{\Gamma_{\mathrm{inout}}} \big(p^2 + c^2\langle u, n\rangle^2\big)\, d\Gamma = 0, \tag{41}$$

which can be seen by substituting $v = u$, $q = p$ into equation (40), using the product rule, and integrating by parts.

Let $v = u^*$, $q = -p^*$ in (40) for some arbitrary smooth functions u^* and p^* (these will later be chosen to satisfy the adjoint equation). Integrating in time over an interval $(0, T)$ yields

$$\begin{aligned} 0 = c\int_0^T\int_\Omega \langle u^*, \partial_t u + \nabla p\rangle\, dx\, dt - \frac{1}{c}\int_0^T\int_\Omega p^*(\partial_t p + c^2 \mathrm{div}\, u)\, dx\, dt \\ + c\int_0^T\int_{\Gamma_{\mathrm{s}}} p^*\langle u, n\rangle\, d\Gamma\, dt - \frac{1}{2}\int_0^T\int_{\Gamma_{\mathrm{inout}}} (p^* + c\langle u^*, n\rangle)(p - c\langle u, n\rangle)\, d\Gamma\, dt \\ + \int_0^T\int_{\Gamma_{\mathrm{in}}} (p^* + c\langle u^*, n\rangle) g\, d\Gamma\, dt. \end{aligned} \tag{42}$$

Now assume that the domain Ω is perturbed by domain variations generated by a vector field V, chosen as described above. We denote by subscript ϵ on the state and costate variables the solutions associated with the perturbed domain Ω^ϵ. Differentiating equation (42) with respect to a domain variation generated by V results in

$$
\begin{aligned}
0 = {} & c\frac{d^+}{d\epsilon}\int_0^T \int_{\Omega^\epsilon} \langle u_\epsilon^*, \partial_t u_\epsilon + \nabla p_\epsilon\rangle \, dx\, dt\Big|_{\epsilon=0} \\
& - \frac{1}{c}\frac{d^+}{d\epsilon}\int_0^T \int_{\Omega^\epsilon} p_\epsilon^*(\partial_t p_\epsilon + c^2 \mathrm{div}\, u_\epsilon)\, dx\, dt\Big|_{\epsilon=0} + c\frac{d^+}{d\epsilon}\int_0^T \int_{\Gamma_{\mathrm{s}}^\epsilon} p_\epsilon^* \langle u_\epsilon, n\rangle \, d\Gamma\, dt\Big|_{\epsilon=0} \\
& - \frac{1}{2}\frac{d^+}{d\epsilon}\int_0^T \int_{\Gamma_{\mathrm{inout}}} (p_\epsilon^* + c\langle u_\epsilon^*, n\rangle)(p_\epsilon - c\langle u_\epsilon, n\rangle)\, d\Gamma\, dt\Big|_{\epsilon=0} \\
& + \frac{d^+}{d\epsilon}\int_0^T \int_{\Gamma_{\mathrm{in}}} (p_\epsilon^* + c\langle u_\epsilon^*, n\rangle) g \, d\Gamma\, dt\Big|_{\epsilon=0}.
\end{aligned} \tag{43}
$$

Applying formulas (36) and (37), where case (i) applies to Γ_{inout} and Γ_{in} and case (iii) to Γ_{s}, together with the product rule of differentiation and the fact that the shape derivative commutes with time and spatial differentiation, yields that expression (43) expands to

$$
\begin{aligned}
0 = {} & c\int_0^T \int_\Omega \langle u^{*\prime}, \partial_t u + \nabla p\rangle \, dx\, dt - \frac{1}{c}\int_0^T \int_\Omega p^{*\prime}(\partial_t p + c^2 \mathrm{div}\, u)\, dx\, dt \\
& + c\int_0^T \int_{\Gamma_{\mathrm{s}}} p^{*\prime}\langle u, n\rangle \, d\Gamma\, dt - \frac{1}{2}\int_0^T \int_{\Gamma_{\mathrm{inout}}} (p^{*\prime} + c\langle u^{*\prime}, n\rangle)(p - c\langle u, n\rangle)\, d\Gamma\, dt \\
& + \int_0^T \int_{\Gamma_{\mathrm{in}}} (p^{*\prime} + c\langle u^{*\prime}, n\rangle) g \, d\Gamma\, dt \\
& + c\int_0^T \int_\Omega \langle u^*, \partial_t u' + \nabla p'\rangle \, dx\, dt - \frac{1}{c}\int_0^T \int_\Omega p^*(\partial_t p' + c^2 \mathrm{div}\, u')\, dx\, dt \\
& + c\int_0^T \int_{\Gamma_{\mathrm{s}}} p^*\langle u', n\rangle \, d\Gamma\, dt - \frac{1}{2}\int_0^T \int_{\Gamma_{\mathrm{inout}}} (p^* + c\langle u^*, n\rangle)(p' - c\langle u', n\rangle)\, d\Gamma\, dt \\
& + c\int_0^T \int_{\Gamma_{\mathrm{horn}}} \langle V, n\rangle \langle u^*, \partial_t u + \nabla p\rangle \, d\Gamma\, dt \\
& - \frac{1}{c}\int_0^T \int_{\Gamma_{\mathrm{horn}}} \langle V, n\rangle p^*(\partial_t p + c^2 \mathrm{div}\, u)\, d\Gamma\, dt + c\int_0^T \int_{\Gamma_{\mathrm{horn}}} \langle V, n\rangle \, \mathrm{div}\,(up^*)\, d\Gamma\, dt,
\end{aligned} \tag{44}
$$

where the dependency on V of the shape derivatives has been suppressed for brevity.

The first five terms in expression (44) vanish identically since u, p satisfy expression (42). Moreover, provided that u, p, and Γ_{horn} are regular enough, terms 10 and 11 in expression (44) will also vanish identically, due to state equation (6). (A sufficient regularity condition is that u and p as well as their derivatives can be continuously

extended up to Γ_{horn}.) Reducing these terms from expression (44) yields

$$
\begin{aligned}
0 = {} & c\int_0^T\int_\Omega \langle u^*, \partial_t u' + \nabla p'\rangle \,dx\,dt - \frac{1}{c}\int_0^T\int_\Omega p^*(\partial_t p' + c^2 \operatorname{div} u')\,dx\,dt \\
& + c\int_0^T\int_{\Gamma_{\text{s}}} p^*\langle u', n\rangle \,d\Gamma\,dt - \frac{1}{2}\int_0^T\int_{\Gamma_{\text{inout}}} (p^* + c\langle u^*, n\rangle)(p' - c\langle u', n\rangle)\,d\Gamma\,dt \\
& + c\int_0^T\int_{\Gamma_{\text{horn}}} \langle V, n\rangle \operatorname{div}(up^*)\,d\Gamma\,dt.
\end{aligned} \tag{45}
$$

By integrating $\langle u^*, \partial_t u'\rangle$ by parts in time and integrating $\langle u^*, \nabla p'\rangle$ by parts in space, we can write the first term in expression (45) as

$$
\begin{aligned}
c\int_0^T\int_\Omega \langle u^*, \partial_t u' + \nabla p'\rangle \,dx\,dt = {} & c\int_\Omega \langle u'(T), u^*(T)\rangle\,dx - c\int_0^T\int_\Omega \langle u', \partial_t u^*\rangle\,dx\,dt \\
& + c\int_0^T\int_{\partial\Omega} p'\langle u^*, n\rangle\,d\Gamma\,dt - c\int_0^T\int_\Omega p' \operatorname{div} u^*\,dx\,dt,
\end{aligned} \tag{46}
$$

where we have used that $u'|_{t=0}$ and $p'|_{t=0}$ vanish due to the homogeneous initial conditions for state equation (6). Similarly, by integrating $p^*\partial_t p'$ by parts in time and integrating $p^*\operatorname{div} u'$ by parts in space, the second term in expression (45) becomes

$$
\begin{aligned}
\frac{1}{c}\int_0^T\int_\Omega p^*(\partial_t p' + c^2 \operatorname{div} u')\,dx\,dt = {} & \frac{1}{c}\int_\Omega p'(T)p^*(T)\,dx - \frac{1}{c}\int_0^T\int_\Omega p'\partial_t p^*\,dx\,dt \\
& + c\int_0^T\int_{\partial\Omega} \langle u', n\rangle p^*\,d\Gamma\,dt - c\int_0^T\int_\Omega \langle u', \nabla p^*\rangle\,dx\,dt.
\end{aligned} \tag{47}
$$

Substituting expressions (46) and (47) into expression (45) and recombining the terms using that $\partial\Omega = \Gamma_{\text{s}} \cup \Gamma_{\text{inout}}$, we find that

$$
\begin{aligned}
0 = {} & c\int_\Omega \langle u'(T), u^*(T)\rangle\,dx + c\int_0^T\int_\Omega \langle u', -\partial_t u^* + \nabla p^*\rangle\,dx\,dt \\
& - \frac{1}{c}\int_\Omega p'(T)p^*(T)\,dx - \frac{1}{c}\int_0^T\int_\Omega p'(-\partial_t p^* + c^2 \operatorname{div} u^*)\,dx\,dt \\
& + c\int_0^T\int_{\Gamma_{\text{s}}} p'\langle u^*, n\rangle\,d\Gamma\,dt - \frac{1}{2}\int_0^T\int_{\Gamma_{\text{inout}}} \big(p^* - c\langle u^*, n\rangle\big)\big(p' + c\langle u', n\rangle\big)\,d\Gamma\,dt \\
& + c\int_0^T\int_{\Gamma_{\text{horn}}} \langle V, n\rangle \operatorname{div}(up^*)\,d\Gamma\,dt.
\end{aligned} \tag{48}
$$

So far functions p^*, u^* have been arbitrary. However, if we assume that they satisfy

the adjoint system

$$
\begin{aligned}
-\frac{\partial u^*}{\partial t} + \nabla p^* &= 0 && \text{in } \Omega \text{ for } t < T,\\
-\frac{\partial p^*}{\partial t} + c^2 \operatorname{div} u^* &= 0 && \text{in } \Omega \text{ for } t < T,\\
\frac{1}{2}\left(p^* - c\langle u^*, n\rangle\right) &= \frac{1}{2}\left(p + c\langle u, n\rangle\right) && \text{on } \Gamma_{\text{in}} \text{ for } t < T,\\
\frac{1}{2}\left(p^* - c\langle u^*, n\rangle\right) &= 0 && \text{on } \Gamma_{\text{out}} \text{ for } t < T,\\
\langle u^*, n\rangle &= 0 && \text{on } \Gamma_{\text{wall}} \cup \Gamma_{\text{symm}} \text{ for } t < T,\\
u^* &\equiv 0 && \text{in } \Omega \text{ at } t = T,\\
p^* &\equiv 0 && \text{in } \Omega \text{ at } t = T,
\end{aligned}
\tag{49}
$$

expression (48) reduces to

$$
\frac{1}{2}\int_0^T \int_{\Gamma_{\text{in}}} \left(p + c\langle u, n\rangle\right)\left(p' + c\langle u', n\rangle\right) d\Gamma\, dt = c\int_0^T \int_{\Gamma_{\text{horn}}} \langle V, n\rangle \operatorname{div}\left(up^*\right) d\Gamma\, dt, \tag{50}
$$

which, combined with expression (39), means that the shape derivate can be given by the integral representation

$$
dJ(\Gamma_{\text{horn}})[V] = 2c\int_0^T \int_{\Gamma_{\text{horn}}} \langle V, n\rangle \operatorname{div}\left(up^*\right) d\Gamma\, dt. \tag{51}
$$

Remark 4. The shape derivative representation can also be written as

$$
dJ(\Gamma_{\text{horn}})[V] = 2c\int_0^T \int_{\Gamma_{\text{horn}}} \langle V, n\rangle \operatorname{div}\left(u^*p\right) d\Gamma\, dt. \tag{52}
$$

This alternative expression can be derived as follows:

$$
\begin{aligned}
&\int_0^T \int_{\Gamma_{\text{horn}}} \langle V, n\rangle \operatorname{div}\left(up^*\right) d\Gamma\, dt = \int_0^T \int_{\Gamma_{\text{horn}}} \langle V, n\rangle \left(\langle u, \nabla p^*\rangle + p^* \operatorname{div} u\right) d\Gamma\, dt\\
&= \int_0^T \int_{\Gamma_{\text{horn}}} \langle V, n\rangle \left(\langle u, \partial_t u^*\rangle - \frac{1}{c^2} p^* \partial_t p\right) d\Gamma\, dt\\
&= -\int_0^T \int_{\Gamma_{\text{horn}}} \langle V, n\rangle \left(\langle \partial_t u, u^*\rangle - \frac{1}{c^2} \partial_t p^* p\right) d\Gamma\, dt\\
&= \int_0^T \int_{\Gamma_{\text{horn}}} \langle V, n\rangle \left(\langle \nabla p, u^*\rangle + p \operatorname{div} u^*\right) d\Gamma\, dt = \int_0^T \int_{\Gamma_{\text{horn}}} \langle V, n\rangle \operatorname{div}\left(pu^*\right) d\Gamma\, dt,
\end{aligned}
\tag{53}
$$

where the state (6) and adjoint (49) equations have been used in the second and fourth equalities, and integration by part in time in the third equality, where also the homogeneous initial (or terminal) conditions for u, u^*, p, and p^* have been exploited.

REFERENCES

[1] S. G. Amin, M. H. M. Ahmed, and H. A. Youssef, *Computer-aided design of acoustic horns for ultrasonic machining using finite-element analysis*, J. Materials Process. Tech., 55 (1995), pp. 254–260.

[2] E. Arian and S. Ta'asan, *Analysis of the Hessian for Aerodynamic Optimization: Inviscid Flow*, Technical Report 96-28, Institute for Computer Applications in Science and Engineering (ICASE), 1996.
[3] E. Bängtsson, D. Noreland, and M. Berggren, *Shape optimization of an acoustic horn*, Comput. Methods Appl. Mech. Engrg., 192 (2003), pp. 1533–1571.
[4] R. Barbieri, N. Barbieri, and K. F. de Lima, *Some applications of the PSO for optimization of acoustic filters*, Appl. Acoustics, 80 (2015), pp. 62–70.
[5] M. P. Bendsøe and O. Sigmund, *Topology Optimization—Theory, Methods and Applications*, 2nd ed., Springer, Berlin, Heidelberg, New York, 2004.
[6] R. Berbieri and N. Barbieri, *Acoustic horns optimization using finite elements and genetic algorithm*, Appl. Acoustics, 74 (2013), pp. 356–363, doi:10.1016/j.apacoust.2012.09.007.
[7] M. Berggren, *A unified discrete-continuous sensitivity analysis method for shape optimization*, in Applied and Numerical Partial Differential Equations, Comput. Methods Appl. Sci. 15, Springer, New York, 2010, pp. 25–39.
[8] D. J. Brackett, I. A. Ashcroft, and R. J. M. Hague, *Multi-physics optimisation of "brass" instruments—A new method to include structural and acoustical interactions*, Struct. Multidiscip. Optim., 40 (2009), p. 611–624, doi:10.1007/s00158-009-0394-0.
[9] L. Chen, *Mesh smoothing schemes based on optimal Delaunay triangulations*, in Proceedings of the 13th International Meshing Roundtable, Williamsburg, VA, 2004, Sandia National Laboratories, pp. 109–120.
[10] M. Colloms, *High Performance Loudspeakers*, 6th ed., Wiley, New York, 2005.
[11] M. C. Delfour and J.-P. Zolésio, *Shapes and Geometries. Metrics, Analysis, Differential Calculus, and Optimization*, 2nd ed., Adv. Des. Control 22, SIAM, Philadelphia, 2011.
[12] Q. Du, V. Faber, and M. Gunzburger, *Centroidal Voronoi tessellations: Applications and algorithms*, SIAM Rev., 41 (1999), pp. 637–676, doi:10.1137/S0036144599352836.
[13] B. Farhadinia, *Structural optimization of an acoustic horn*, Appl. Math. Modeling, 36 (2012), pp. 2017–2030, doi:10.1016/j.apm.2011.08.016.
[14] J. S. Hesthaven and T. Warburton, *Nodal Discontinuous Galerkin Methods. Algorithms, Analysis, and Applications*, Texts Appl. Math. 54, Springer, New York, 2008, doi:10.1007/978-0-387-72067-8.
[15] R. M. Hicks and P. A. Henne, *Wing design by numerical optimization*, J. Aircraft, 15 (1978), pp. 407–412.
[16] F. Kasolis, E. Wadbro, and M. Berggren, *Fixed-mesh curvature-parameterized shape optimization of an acoustic horn*, Struct. Multidiscip. Optim., 46 (2012), pp. 727–738, doi:10.1007/s00158-012-0828-y.
[17] A. Logg, K.-A. Mardal, and G. N. Wells, eds., *Automated Solution of Differential Equations by the Finite Element Method*, Lect. Notes Comput. Sci. Eng., Springer, New York, 2012, doi:10.1007/978-3-642-23099-8.
[18] R. C. Morgans, A. C. Zander, C. H. Hansen, and D. J. Murphy, *EGO shape optimization of horn-loaded loudspeakers*, Optim. Engrg., 9 (2008), pp. 361–374.
[19] P. M. Morse, *Vibration and Sound*, McGraw–Hill, New York, 1948.
[20] D. Noreland, R. Udawalpola, and M. Berggren, *A hybrid scheme for bore design optimization of a brass instrument*, J. Acoust. Soc. Amer., 128 (2010), pp. 1391–1400, doi:10.1121/1.3466871.
[21] D. Noreland, R. Udawalpola, P. Seoane, E. Wadbro, and M. Berggren, *An Efficient Loudspeaker Horn Design by Numerical Optimization: An Experimental Study*, Technical Report UMINF 10.01, Department of Computing Science, Umeå University, 2010.
[22] S. W. Rienstra and A. Hirschberg, *An Introduction to Acoustics*, revised and updated version of reports IWDE 92-06 and IWDE 01-03, Eindhoven University of Technology, Eindhoven, The Netherlands, 2015.
[23] S. Schmidt, *Efficient Large Scale Aerodynamic Design Based on Shape Calculus*, Ph.D. thesis, Department of Mathematics, University of Trier, Germany, 2010.
[24] S. Schmidt, *A Two Stage CVT/Eikonal Convection Mesh Deformation Approach for Large Nodal Deformations*, preprint, arXiv:1411.7663, 2014.
[25] S. Schmidt, C. Ilic, V. Schulz, and N. Gauger, *Three dimensional large scale aerodynamic shape optimization based on shape calculus*, AIAA J., 51 (2013), pp. 2615–2627, doi:10.2514/1.J052245.
[26] S. Schmidt and V. Schulz, *Impulse response approximations of discrete shape Hessians with application in CFD*, SIAM J. Control Optim., 48 (2009), pp. 2562–2580, doi:10.1137/080719844.
[27] S. Schmidt and V. Schulz, *A* 2589 *line topology optimization code written for the graphics card*, Comput. Vis. Sci., 14 (2011), pp. 249–256, doi:10.1007/s00791-012-0180-1.

[28] J. Sokolowski and J.-P. Zolésio, *Introduction to Shape Optimization: Shape Sensitivity Analysis*, Springer, Berlin, Heidelberg, 1992.
[29] S. Ta'asan, *One-shot methods for optimal control of distributed parameter systems* I: *Finite dimensional control*, ICASE, Technical Report 91-2, 1991.
[30] R. Udawalpola and M. Berggren, *Optimization of an acoustic horn with respect to efficiency and directivity*, Internat. J. Numer. Methods Engrg., 73 (2008), pp. 1571–1606.
[31] R. Udawalpola, E. Wadbro, and M. Berggren, *Optimization of a variable mouth acoustic horn*, Internat. J. Numer. Methods Engrg., 85 (2011), pp. 591–606, doi:10.1002/nme.2982.
[32] E. Wadbro and M. Berggren, *Topology optimization of an acoustic horn*, Comput. Methods Appl. Mech. Engrg., 196 (2006), pp. 429–436.
[33] E. Wadbro, R. Udawalpola, and M. Berggren, *Shape and topology optimization of an acoustic horn-lens combination*, J. Comput. Appl. Math., 234 (2010), pp. 1781–1787.
[34] B. Webb and J. Baird, *Advances in line array technology for live sound*, in Proceedings of the 18th Audio Engineering Society Conference: Live Sound, 2003, 10.